

Rodent retinal circulation organization and oxygen metabolism revealed by visible-light optical coherence tomography

SHAOHUA PI, ACNER CAMINO, XIANG WEI, JOSEPH SIMONETT, WILLIAM CEPURNA, DAVID HUANG, JOHN C. MORRISON, AND YALI JIA*

Casey Eye Institute, Oregon Health & Science University, Portland, OR, USA

*jia.y@ohsu.edu

Abstract: Visible light optical coherence tomography (vis-OCT) is an emerging label-free and high-resolution 3-dimensional imaging technique that can provide retinal oximetry, angiography, and flowmetry in one modality. In this paper, we studied the organization of the arterial and venous retinal circulation in rats using vis-OCT. Arterioles were found predominantly in the superficial vascular plexus whereas veins tended to drain capillaries from the deep capillary plexus. After that, we determined the oxygen metabolic rate supported by retinal microcirculation by combining retinal vessel oxygen saturation and blood flow measurements. The ability to visualize and monitor retinal circulation organization and oxygen metabolism by vis-OCT may provide new opportunities for understanding the pathology of ocular diseases.

© 2018 Optical Society of America under the terms of the [OSA Open Access Publishing Agreement](#)

1. Introduction

Blood flow within the retinal vasculature supplies metabolites (oxygen, glucose and other nutrients) to the retinal layers and disposes of waste products [1]. In the retina, the major vessels run from the posterior pole to the periphery to nourish the entire retina. Depending on tissue oxygen demand and other metabolic needs, the number of laminar layers differs among animals and even in different retinal regions [2]. Either all or combinations of a total of four vascular complexes have been histologically observed in the human and animal retinas [3]. These vascular networks include a nerve fiber layer plexus (NFLP), a ganglion cell layer plexus (GCLP), an intermediate capillary plexus (ICP) at the inner border of inner nuclear layer, and a deep capillary plexus (DCP) at the outer border of the inner nuclear layer. Because they support the high metabolic demand of the neuroretina, a detailed understanding of the structural and functional characteristics of the retinal vasculature is of utmost interest in understanding retinal physiology and pathology.

Fluorescein angiography has for years been the gold standard used to visualize the retinal vasculature close to the vitreoretinal interface, yet it does not provide reliable information on the 3-dimensional (3D) microcirculatory architecture [4]. Vascular corrosion casting integrated with tissue maceration and scanning electron-microscopy (SEM) can reveal retinal microvascular connections but can only be performed *in vitro* [3]. Recent advances in optical coherence tomographic angiography (OCTA) [5–8] have succeeded in non-invasively visualizing the above-mentioned 3D retinal microvasculature with four distinct retinal capillary plexuses [2]. Since arteries and veins can only be reliably distinguished by their directions of blood flow or the difference in oxygen saturation, conventional OCTA lacks the ability to differentiate arterial versus venous connections to these capillary beds. This limitation impairs OCTA's ability to achieve a detailed functional understanding of these structures.

The recent advent of visible light OCT (vis-OCT) [9] allows retinal oximetry [10,11] with enhanced extinction coefficient contrast between oxy- and deoxy- hemoglobin [12], as well as

the retinal angiography and retinal flowmeter by Doppler OCT [13,14], which had been accomplished previously in near infrared OCT. Although the technique has been successfully applied to human retina [15,16] and other tissue [17] imaging, its great potential on retinal imaging by combining all these functional features have not been fully investigated. We have established a fiber-based vis-OCT with high axial resolution [18] and previously performed automated retinal oximetry with good reproducibility [19]. Our hypothesis for this study was that vis-OCT could enable noninvasive visualization of the organization of the retinal circulation and measurement of oxygen metabolism supported by retinal circulation. We proposed to combine a full set of functional features (i.e. retinal oximetry, angiography and flowmetry) of vis-OCT to verify this hypothesis in the Brown Norway rat.

2. Method

2.1 Animal preparation

Brown Norway rats (17 weeks old, n = 8) were initially anesthetized with 5% isoflurane in a sealed box for 10 minutes, followed by 2.5% isoflurane during the imaging session. Pure oxygen (100% O₂) with flow rate at 1 L/min was ventilated for inhalation. Under anesthesia, the animal was immobilized in a custom-made imaging stage with multidimensional manipulation for alignment. The pupil was dilated with 1% tropicamide ophthalmic solution before imaging. To keep the cornea moist, sterile irrigating salt solution (Alcon Laboratories Inc.) was applied to the eye every other minute. The animal's body temperature was maintained with a 38.5 °C water-warming blanket. The exhaust gas, including isoflurane, was removed by a vacuum pump to avoid carbon dioxide accumulation and collected by an anesthesia gas filter (OMNICON F/air, Bickford [20]) before releasing to the open air.

All experimental procedures complied with the Association for Research in Vision and Ophthalmology Statement for the Use of Animals in Ophthalmic and Vision Research and were approved by the Institutional Animal Care and Use Committee (IACUC) of the Oregon Health & Science University (OHSU).

2.2 Image acquisition

The vis-OCT used in this work is a custom-built prototype [18] housed in the Center for Ophthalmic Optics & Lasers Laboratory (COOL LAB) [21] of OHSU. The spectrum covered the high absorption contrast region of hemoglobin from 510 nm to 610 nm ($\lambda_c = 560$ nm, full width at half maximum (FWHM) was ~90nm) and was calibrated with a neon calibration light source (NE-1, Ocean Optics [22]). The dispersion mismatch between the two arms was compensated both physically and numerically. An unbalanced 90:10 wideband fiber optical coupler delivered 10% power into the sample arm (power = 0.8 mw). A telescope tube ($f_1 = 75$ mm, $f_2 = 11$ mm) (Fig. 1(A)) guided light into the rat eye, with rat head immobilized on a device allowing oxygen inhalation and carbon dioxide removal (Fig. 1(B)). The system operated at a flexible axial scan sampling rate and scanning angle, with a 1.2-μm axial resolution and approximately 6-μm lateral resolution with an image depth of 1.8 mm. The maximum sensitivity was measured as 89 dB with a protected silver mirror.

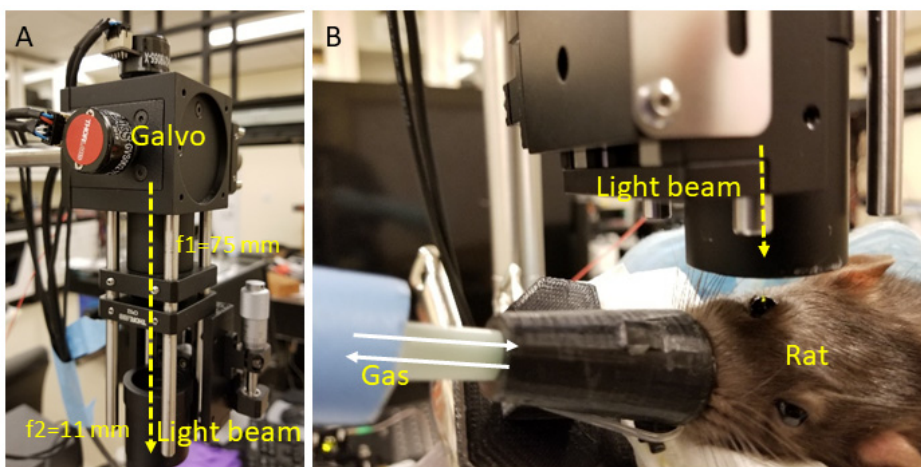


Fig. 1. Experimental setup of sample arm illustrates how rat eye was scanned. (A) The sample arm was fixed with light beam illuminated vertically. (B) The rat was scanned vertically with its head immobilized on a customized gas inhalation device.

Volumetric raster scans were collected at $\pm 3^\circ$ scanning angle at 2-D galvo mirror, resulting in a $3.2 \text{ mm} \times 3.2 \text{ mm}$ image field on the rat retina ($d_{\text{eyeball}} = 6.2 \text{ mm}$). In the fast transverse (X) scanning direction, 512 axial scans were sampled to form a B-scan, resulting in the sampling density of $6.25 \mu\text{m}/\text{line}$. The consecutive B-scans were captured before moving to the next slow axis (Y) position. A total of 512 Y positions were sampled within 17 seconds at the A-scan rate of 50 kHz and B-scan rate of 88 Hz.

To obtain the wide field reflectance and angiographic images shown here, the optic disc was first placed at the center of the field of view and a volumetric raster scan was taken for reference. Then the rat was tilted and its optic disc was placed at each of the corners of field of view consecutively to take volumetric raster scans on the inferior-nasal, inferior-temporal, superior-temporal, superior-nasal regions.

In addition, two concentric circular scans ($r_1 = 0.6 \text{ mm}$, $r_2 = 0.8 \text{ mm}$) consisting of 4096 A-lines ($\sim 1 \mu\text{m}/\text{line}$) were also acquired around the optic disc, transecting all major retinal arteries and veins for the purpose of blood flow measurement and arteriovenous identification by flow direction. The scans were repeated 30 times to account for arterial blood flow differences during systole and diastole of the cardiac cycle. Three repeated scans were acquired within minutes to reduce measurement variation.

2.3 Oxygen saturation

The spatial- and depth-resolved optical density $OD(z, \lambda)$ is defined as the logarithm of the ratio of the reflected intensity spectrum $I(z, \lambda)$ to the source spectrum $I_0(\lambda)$. It stands for the reflectivity ability at a certain illumination wavelength for the tissue at a certain depth and can be expressed as Eq. (1) based on a modified Beer's law [10]. Basically, d is the accumulated absorption length for the voxels in depth. The scattering spectrum of the vessel wall $r(\lambda)$ can be modeled as a power law $A \cdot \lambda^{-\alpha}$ under the first-order Born approximation [23]. The scattering spectrum at the reference arm R_0 is considered as a wavelength-independent constant. The subscript HbO_2 and Hb indicate the contribution from oxygenated and deoxygenated hemoglobin respectively, with their extinction coefficients ε referring to the literature [12] and concentrations C being calculated by fitting, in order to find the oxygen saturation $sO_2 = C_{HbO_2} / (C_{HbO_2} + C_{Hb})$.

$$OD(z, \lambda) = \ln\left(\frac{I(z, \lambda)}{I_0(\lambda)}\right) = -2d \left[C_{HbO_2} \varepsilon_{HbO_2}(\lambda) + C_{Hb} \varepsilon_{Hb}(\lambda) \right] + \ln(r(\lambda)) + \ln(R_0) \quad (1)$$

The $OD(z, \lambda)$ can be extracted by short time Fourier transform (STFT) spectroscopic analysis of the interference fringes. Vessel posterior voxels were selected automatically for analysis [19]. A Gaussian window with a full-width at half-maximum of approximately 9 nm and an interval distance around 3 nm were applied, resulting in 21 split spectral bands in total. Only those bands within the contrast region from 527 nm to 582 nm were selected for linear regression fitting.

2.4 Angiography

The recorded data were analyzed with the SSADA algorithm [5] for angiography. Briefly, the algorithm splits the full spectrum into multiple bands and calculates the decorrelation value among consequent B-scans at each band. After that, the contrast of the motion-based angiogram is largely enhanced by averaging the results from all bands. Layer segmentation was done with a graph-search technique [24] on structural B-scan images. The laminar vascular/capillary plexuses were then generated by projecting the flow signal within specific slabs. *En face* angiograms at the four scanning regions were montaged together for a wide field of view (~60 degree). Note that only a circular region with the diameter of 5 mm was highlighted for visualization.

Projected *en face* angiograms from the superficial vascular plexus was enhanced by a Frangi multiscale vessel filter [25]. Vessel binary masks were obtained by setting a threshold to the enhanced angiogram. After that, morphologic processing was performed to retain only vessel information. After tracing the vascular network for each major vessel, the vessel binary mask could be further isolated into an artery and a vein binary mask according to the measured oxygen saturation in each major vessel. Vessel density was calculated separately for arteries and veins as the ratio of the vascular area to the total area.

2.5 Blood flow

The blood flow F ($\mu\text{L}/\text{min}$) (Eq. (2)) for each major vessel was obtained by the product of the averaged vessel blood flow velocity \bar{v} (mm/s) and its cross-section area S that is perpendicular to the flow direction [13]

$$F = \bar{v} \cdot S \quad (2)$$

The distribution of blood flow velocity can be expressed as Eq. (3) and obtained from the phase-sensitive Doppler OCT analysis to the circular scans. Briefly, the $\Delta\varphi$ is the Doppler phase shift between adjacent A-lines in the B-scan with ultra-high sampling density. The sampling rate f_s of the charged coupled device (CCD) camera is 50 kHz. The center wavelength of the light spectrum λ_0 is 565 nm. Refractive index n of the retina is taken as 1.4 [26]. The Doppler angle θ [rad] was calculated from the vessel position shifts between the inner circular scan and outer circular scan. Vessel diameter H was measured axially from B-scan images.

$$v = \frac{f_s \lambda_0 \Delta\varphi}{4\pi n \cos(\theta)} \quad S = \frac{\pi}{4} H^2 \sin(\theta)^2 \quad (3)$$

2.6 Retinal oxygen metabolic rate

Oxygen metabolic rate is defined as the oxygen consumption of the tissue over time, which can be deduced from the difference of oxygen content supplied by arteries and carried away by veins per unit time [27]. In the inner retina, the oxygen demand is mainly supplied by the retinal circulation, where all vessels originate from the central retinal artery and vein, which enter the eye with the optic nerve. Thus the rMRO₂ (g/min) can be quantified as

$$rMRO_2 = \frac{4W_{O_2}}{W_{HbO_2}} \cdot C_{HbT} \cdot \left(\sum_i sO_{2a} F_{a,i} - \sum_i sO_{2v} F_{v,i} \right) \quad (4)$$

Where W_{O_2} and W_{HbO_2} are the molecular weights of O_2 [32 g/mol] and oxygenated hemoglobin [68000 g/mol] respectively. One oxygenated hemoglobin can bind 4 oxygen molecules. The total hemoglobin concentration in blood C_{HbT} is 150 g/L for rat. The sO_2 and F are the measured oxygen saturation and blood flow in each vessel respectively. The subscripts a and v denote the contribution of oxygen transported in from the artery and transported out by the vein respectively, i indicates vessel index and the difference between the two transport rates is considered to be the amount consumed by retinal metabolism.

3. Results

3.1 Organization of retinal circulation

From the cross-sectional B-scan and the averaged A-line profile (Fig. 2(A)), the distinct retinal structural layers and three vascular plexuses were observed. In Brown Norway rats, the retinal microvasculature originates from the central retinal artery and central retinal vein, which enter the eye just inferior to the optic nerve. They both branch into several major retinal vessels in a “spoke wheel” distribution radiating towards the retinal periphery (Fig. 2(B)-2(C)). The rat eye lacks a fovea, and therefore has no foveal avascular zone.

The capillaries in the ICP (Fig. 2(D)) and DCP (Fig. 2(E)) follow curvilinear and tortuous paths just as they do in humans, and are evenly distributed over the imaging area. Each plexus possesses a unique distribution pattern, indicating a successful illustration of the laminar vascular plexuses with vis-OCT. Compared to the human retina [2], the vascular patterns are less dense and do not demonstrate radial peripapillary capillaries (Fig. 2(C)).

On the SVP angiogram with isolated vessel trees color-coded with oxygen saturation of major vessels (Fig. 2(F)), we found major arteries ($sO_2 > 93\%$, red) were located on the top of major veins ($sO_2 < 93\%$, green), and they are interleaved. Arterioles and their branches were predominately distributed extensively within the SVP. The minimal vessel calibers in the *en face* images in this study were about $\sim 12 \mu m$, which is similar to the diameter of smallest capillaries. Branches down to the 5th order could be visualized and, even at this level, relatively few direct connections between arterial and venous branches were observed (e.g. white arrow in Fig. 2(C)). Precapillary arterioles tend to branch in a dichotomous way before disappearing from the SVP slab. By contrast, fewer venules were present in the SVP and they tended to travel only a short distance within this slab. This difference could be demonstrated by measuring vessel density in vessel binary masks of arteries and veins separately. In this study, SVP vessel densities were $\sim 17\%$ and $\sim 6\%$ for arteries and veins, respectively.

The reason veins have less perfusion area than arteries in the SVP is that their branches tend to vertically connect with DCP, which can be better visualized by overlaying the SVP on the DCP (Fig. 2(G)). In this representative case, nineteen remarkable venule interconnections were indicated by arrows, illustrating that veins primarily drain blood from the DCP. Some venules are connected to veins vertically, while others are oblique and travel a certain path before being collected by major veins in the SVP.

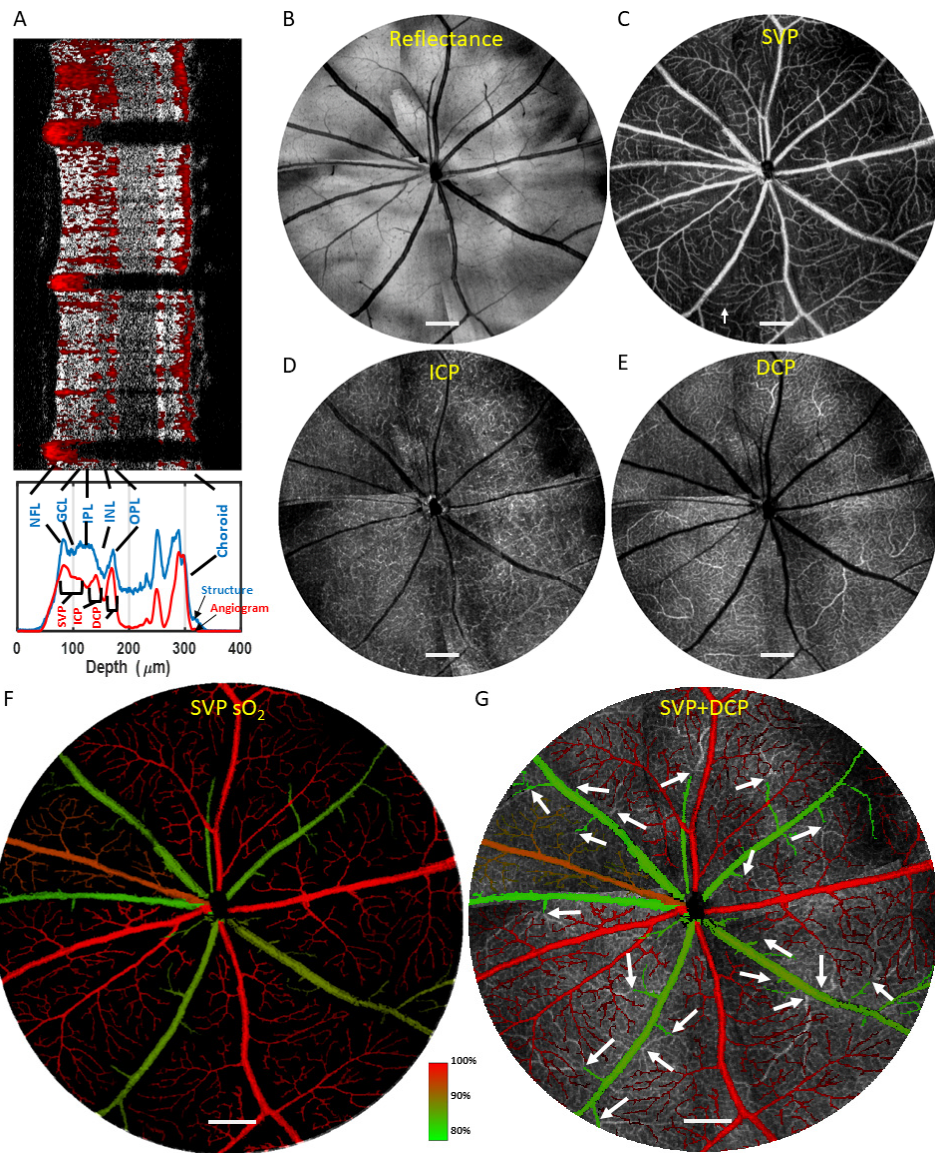


Fig. 2. Ultra wide-field *en face* images (diameter = 5 mm) stitched from four 3.2 mm × 3.2 mm volumetric scans in the superior, nasal, inferior and temporal regions respectively. Scale bar = 500 μm . (A) Cross-sectional structural B-scan overlaid with angiogram (upper panel), and averaged depth profiles demonstrating the positions of the retinal layers and vascular plexuses (lower panel). NFL: nerve fiber layer, GCL: ganglion cell layer, IPL: inner plexiform layer, INL: inner nuclear layer, OPL: outer plexiform layer. SVP: superficial vascular plexus, ICP: intermediate capillary plexus, DCP: deep capillary plexus. (B) Reflectance *en face* image was generated by mean projection of OCT signal within the retinal slab. (C) SVP *en face* image were generated by maximum projection of angiogram. White arrow indicates a direct connection from artery to vein. (D) ICP *en face* image were generated by maximum projection of angiogram. (E) DCP *en face* image were generated by maximum projection of angiogram. (F) Arteriovenous identification (arteries: red, veins: green) in the SVP of the rat retina by oxygen saturation at 100% O₂ inhalation. The arterial vasculature extends over the majority of the SVP and its vessel density is almost 3 times that of the venous vasculature. (G) DCP (gray scale, E) overlaid with SVP (color-coded by sO₂, F) demonstrates venules crossing between plexuses, indicating veins drain blood flow from the DCP. The remarkable venules connection between DCP and SVP are annotated by white arrows. Note some venules in SVP are obliquely crossing to the DCP, while others are vertically crossing to the DCP.

3.2 Oxygen metabolism

Through the dual circles Doppler scans (Fig. 3(A)-3(C)), we observed that both arteries and veins can be distinguished based on their flow directions (Fig. 3(D)), consistent with the differentiation made by oxygen saturation. It should be noted that the locations for Doppler OCT should be carefully selected, because the angle between the OCT beam and direction of blood flow is needed and the opposite flow direction is required for this purpose. We also found the values of the velocity are higher in the center of vessels than in the regions near to the vessel walls, in agreement with the expected parabolic blood flow velocity distribution across large vessels.

Retinal blood oxygen transport rate ($r\text{TRO}_2$) was obtained by determining the amount of oxygen transportation per unit time through sO_2 and blood flow (Fig. 3(E)-3(F)). The retinal oxygen metabolic rate (Fig. 3(G)) is measured as $261.7 \pm 49.2 \text{ ng/min}$ from $n = 8$ eyes, which can be converted to $187.9 \pm 35.3 \text{ nL/min}$ by the ideal gas law [27]. The measured values suggest that $r\text{MRO}_2$ in hyperoxia condition is equivalent to that in normal air and lower than that in hypoxic conditions [28].

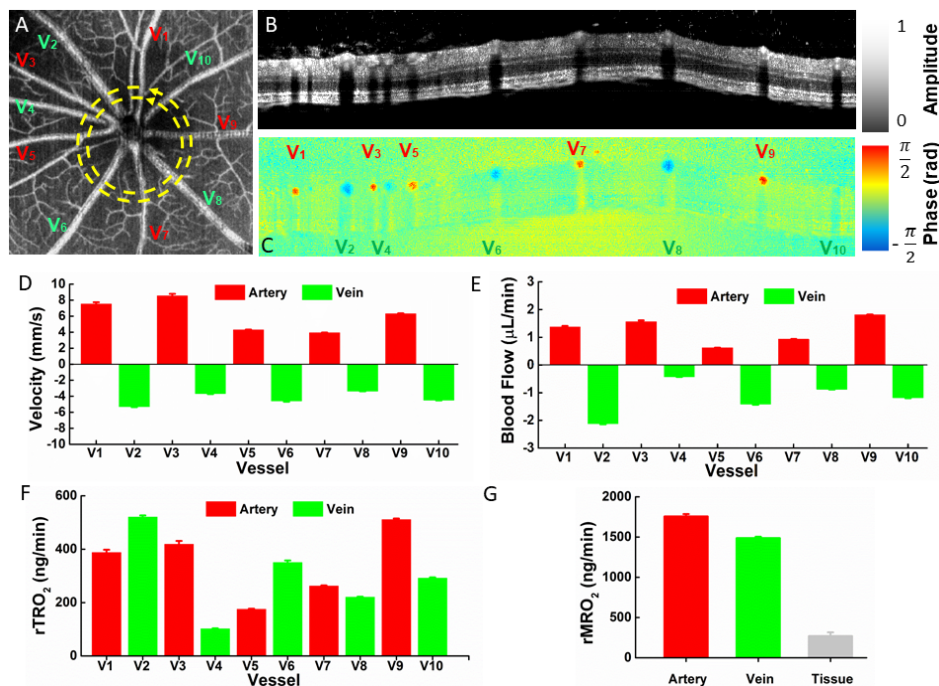


Fig. 3. Retinal oxygen metabolism rate measurement with visible light OCT. (A) *en face* angiogram of the superficial vascular plexus near the optic disc region labeled by vessel number (red: artery, green: vein) and dual concentric Doppler circular scan positions (yellow dash line, arrow: scan direction). (B) Structural B-scans visualize major retinal vessels. (C) Doppler phase shift image differentiates arteries (red) from veins (blue), which supports the arteriovenous identification results by retinal oximetry using vis-OCT. (D) Blood flow velocity, (E) blood flow and (F) blood oxygen transport rate for each vessel with standard deviation calculated on three repeated dual circular scans. (G) Retinal oxygen metabolism is calculated by the subtraction of the total arterial oxygen transport rate minus the total venous oxygen transport rate with measurement repeatability of $\sim 40 \text{ ng/min}$.

4. Discussion

New functional OCT modalities are allowing researchers to gain better insight into the pathophysiology of ocular diseases. Previous OCTA research suggested that ischemia is part of the causal chain in many leading causes of blindness [29]. However, how the retinal

circulation is organized, how oxygenation differs between retinal plexuses and which plexuses are more vulnerable to ischemia are still unclear. Since vis-OCT can provide maps of the retinal circulation in three dimensions together with vessel oxygen saturation with excellent reproducibility [19], it stands as an instrument with a great potential to help address these questions.

One of the current debates in which vis-OCT exhibits potential to elucidate some clarity is that of whether retinal plexuses drain through venous flow independently, or if this drainage is primarily through the DCP. Previously, both vertical inter-plexus and horizontal intra-plexus arteriovenous connections had been observed by our group in human retinas with projection-resolved OCTA techniques [30]. Yet a debate on the organization of retinal circulation still exists [31], and a hybrid pattern has gradually become more convincing, with more details recently revealed by OCTA [32]. However, given the very dense vascular network (60%~80% vessel density in SVP) in the human retina, the architecture of its microvasculature remains unclear at limited resolution.

Here in the rat eye, the retinal microvasculature could be visualized more clearly using our vis-OCT technique for four main reasons. First, vis-OCT enables rapid and accurate identification of arterioles and venules by oxygen saturation. This helps differentiate the vascular type so that we can delineate the arterial and venous networks separately. Second, the axial and transverse resolutions of our prototype vis-OCT are improved with respect to conventional infrared OCT [18]. Third, the vascular patterns in the rat retina are relatively sparse (~25% vessel density in SVP) compared to human retina. Fourth, with a greater distance from the optic disc reached by ultra-wide field angiography, more vascular features can be visualized.

Researchers have previously explored the 3D connectivity of rat retina circulation using OCT angiography [33]. They demonstrated the dense connectivity between the ICP and DCP by tracing the capillaries. However, they failed to reveal the full landscape of retina vascular architecture due to lack of 1) arteriovenous differentiation results 2) accurate retina layers segmentation, and 3) wide-field of view. From our results above, three features of the rat retinal circulation organization can be concluded. First, the arterial network predominates in the SVP. Second, direct arteriovenous connections in the SVP were seldom observed (white arrow in Fig. 2(C)). Third, that veins drain blood flow primarily through the DCP, where arborescent patterns connecting directly into major venules could be appreciated. The findings are similar to the previously reported ex vivo observations in pig and mouse retinas by confocal microscopy [31,34].

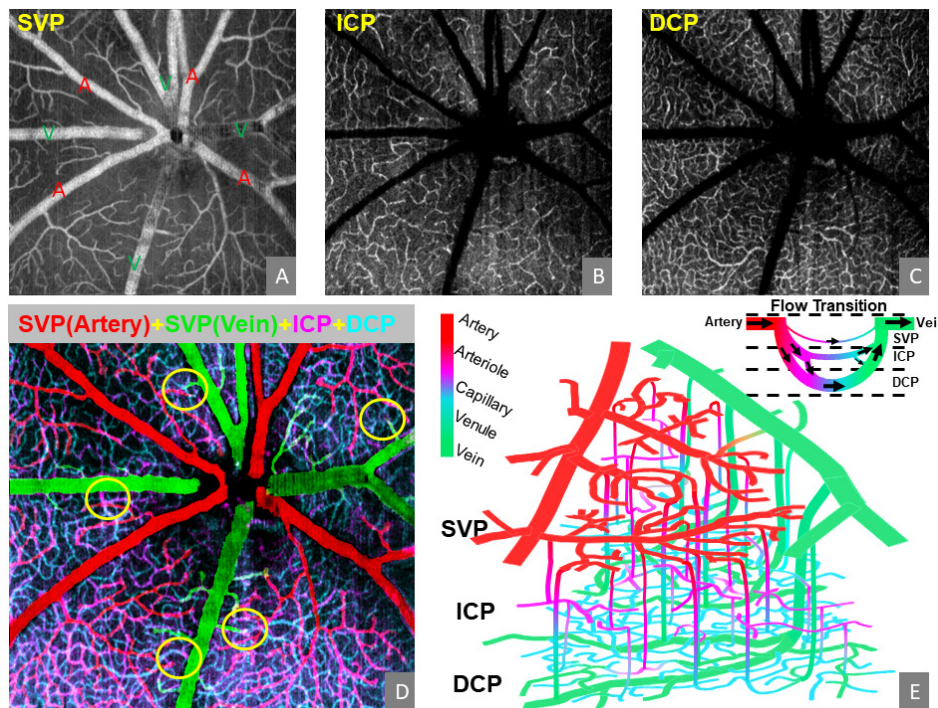


Fig. 4. *En face* images ($2 \times 2 \text{ mm}^2$) of three vascular plexuses (A-C) and overlaid *en face* image (D) with flow drainage through DCP by major veins marked by yellow circles. The 3D schematic vascular network (E) illustrates the flow transition from artery to vein with microvasculature architecture corresponding to the current findings.

Although the capillary connections in the ICP were hard to trace, a reasonable conjecture that the capillaries in the ICP connect to the diving end of arterioles in the SVP could be made through a limited field angiogram centered at the optic disc (Fig. 4(A)-4(D)) and a fly through video (Visualization 1). Based on the findings above, we suggest a predominantly blood flow transition pathway through the DCP in the rat retina (Fig. 4(E)), i.e. the primary flow transition within the microvasculature architecture would be in a way of artery (SVP) \rightarrow arteriole (SVP) \rightarrow capillary (ICP and DCP) \rightarrow venule (DCP) \rightarrow vein (SVP). Nevertheless, direct connections to venules were occasionally observed for capillaries in the ICP at the same point where underlying DCP capillaries drain. This observation, together with the few direct arteriovenous connections observed in the SVP suggest that although serial organization is predominant, the complex vascular distribution is more accurately described by a hybrid model (Fig. 4(E), flow transition schematic). Anatomic differences between species are to be expected, particularly when considering those with a fovea and parafoveal vasculature, and several models of microvascular connectivity in the human retina have been discussed. Some authors have proposed a serial model where venous drainage occurs primarily through vortex-like vessels in the DCP [35]. Others have identified frequent connections between arterioles and venules at each of the retinal capillary plexuses in human retina. The situation suggests a predominantly parallel organization within a hybrid connectivity model [32], resembling the more complicated function of human retina. Additionally, the existence of focal, plexus specific ischemia such as nerve fiber layer infarcts (cotton wool spots) and paracentral acute middle maculopathy would be difficult to explain with a pure serial model in humans and further supports the hybrid model. The high axial resolution of vis-OCT angiography may help further clarify this anatomy.

In addition to vascular mapping, noninvasive measurement of blood flow with vis-OCT in all major retinal vessels allows for calculation of total retinal blood flow, which was 6.5-8

$\mu\text{L}/\text{min}$ per retina in this study with 100% oxygen inhalation. While this value is significantly affected by rat size and anesthesia protocol, our finding fits well with reported value ranges from previous invasive and noninvasive studies [36,37]. There are many potential clinical applications of vis-OCT determined flowmetry. Measuring flow changes over time or between eyes may be useful in the early diagnosis of impending retinal vascular occlusions or ocular ischemic syndrome. A decrease in blood flow in a retinal tumor feeder vessel could be a marker of successful treatment response. Differences in flow between the systolic and diastolic phases of the cardiac cycle may provide information about vessel stiffness and systemic atherosclerosis.

Besides giving access to the arteriovenous flow distribution in the retina, this technology also allowed us to quantify the retinal oxygen metabolic rate, a potential early biomarker for vision-threatening retinal diseases such as diabetic retinopathy, age-related macular degeneration or central retinal vein occlusion. Vis-OCT could also be used to address fundamental pathophysiology questions such as what are the initial hemodynamic dysregulations and early metabolism changes in diabetic retinopathy, where there is current debate due to conflicting data [38,39]. Furthermore, the combination of assessing vascular anatomy, flow rates and oxygen delivery might reveal and explain flow redistributions in diseases of the retinal microvasculature, help explain the dynamics of oxygen supply in the event of unmet metabolic needs, and shed light into the natural history of complications like neovascularization. The outstanding versatility and non-invasiveness of vis-OCT make it a potentially valuable technology for future exploration of these questions.

Safety of exposure to visible light remains a major concern for vis-OCT. Delori *et al* have shown that the visible light is safe at limited exposure duration under certain radiant power [40]. Recently, human retina imaging using vis-OCT was achieved using a much reduced laser power [41,42]. However, this work was performed on normal subjects only. Further improvements in instrument sensitivity and/or advanced image processing will be required in order to diminish discomfort while preserving a reasonable imaging quality before this technology can be applied to patients. The question of whether the light exposure of vis-OCT will directly alter retinal oxygen metabolism or blood flow must also be addressed when considering clinical applications. Previous work suggests that any effect may be minimized at the high scan frequency of vis-OCT and in eyes that are already light adapted [43,44].

Currently, oxygen saturation is only assessable in major retinal vessels. Though it is sufficient to calculate the total oxygen metabolism, the lack of capillary oxygen saturation limits the usefulness of distribution maps of oxygen metabolism, which might be altered in very early stages of ocular diseases. Successful assessment of capillary oxygen saturation currently faces two main challenges: 1) red blood cells pass through the capillary one by one, causing a scattering spectrum that is highly dependent on their geometry, orientation and size [45]. 2) There is limited hemoglobin absorption along the axial direction in capillaries, which is not sufficient to provide enough contrast for oxygen saturation measurement. With the development of vis-OCT technology, these issues may be solved by a more effective oxygen saturation algorithm and/or better laser sources.

5. Conclusion

In summary, three functional features, retinal angiography, oximetry and flowmetry have been combined in the vis-OCT system to image retinal circulation of Brown Norway rats. Using oximetry to help differentiate arteries from veins, we observed a predominance of arterioles in the superficial vascular plexus, whereas venules (the branches of major veins) tended to drain blood from the DCP. This vascular organization suggested a predominantly serial pattern of blood flow transition from arteries to veins in rat's retinal circulation. In addition, the retinal oxygen metabolic rate was also measured by combining retinal oximetry and retinal flowmetry. With these capabilities, future developments based on vis-OCT have

potential to play a crucial role in better understanding abnormalities of retinal microvasculature anatomy and oxygen metabolism in various ocular diseases and disorders.

Funding

R01 EY027833, DP3 DK104397, R01 EY024544, R01 EY023285, R01 EY010145, P30 EY010572 from the National Institutes of Health (Bethesda, MD), and an unrestricted departmental funding grant and William & Mary Greve Special Scholar Award from Research to Prevent Blindness (New York, NY).

Disclosures

David Huang: Optovue Inc (F, I, P, R). Yali Jia: Optovue Inc (F, P). Oregon Health & Science University, Yali Jia, and David Huang have financial interest in Optovue, Inc., a company that may have a commercial interest in the results of this research and technology. These potential conflicts of interest have been reviewed and managed by OHSU. Other authors do not have financial interest in the participant of this article.

References

1. J. H. Parsons, *The Ocular Circulation* (Bale & Danielsson, 1903).
2. J. P. Campbell, M. Zhang, T. S. Hwang, S. T. Bailey, D. J. Wilson, Y. Jia, and D. Huang, "Detailed vascular anatomy of the human retina by projection-resolved optical coherence tomography angiography," *Sci. Rep.* **7**(1), 42201 (2017).
3. H. R. Zhang, "Scanning electron-microscopic study of corrosion casts on retinal and choroidal angioarchitecture in man and animals," *Prog. Retin. Eye Res.* **13**(1), 243–270 (1994).
4. B. Khoobehi and G. A. Peyman, "Fluorescent labeling of blood cells for evaluation of retinal and choroidal circulation," *Ophthalmic Surg. Lasers* **30**(2), 140–145 (1999).
5. Y. Jia, O. Tan, J. Tokayer, B. Potsaid, Y. Wang, J. J. Liu, M. F. Kraus, H. Subhash, J. G. Fujimoto, J. Horngger, and D. Huang, "Split-spectrum amplitude-decorrelation angiography with optical coherence tomography," *Opt. Express* **20**(4), 4710–4725 (2012).
6. K. Kurokawa, K. Sasaki, S. Makita, Y.-J. Hong, and Y. Yasuno, "Three-dimensional retinal and choroidal capillary imaging by power Doppler optical coherence angiography with adaptive optics," *Opt. Express* **20**(20), 22796–22812 (2012).
7. M. Pircher and R. J. Zawadzki, "Review of adaptive optics OCT (AO-OCT): principles and applications for retinal imaging," *Biomed. Opt. Express* **8**(5), 2536–2562 (2017).
8. T. E. de Carlo, A. Romano, N. K. Waheed, and J. S. Duker, "A review of optical coherence tomography angiography (OCTA)," *Int. J. Retina Vitreous* **1**(1), 5 (2015).
9. X. Shu, L. Beckmann, and H. Zhang, "Visible-light optical coherence tomography: a review," *J. Biomed. Opt.* **22**(12), 121707 (2017).
10. J. Yi, Q. Wei, W. Liu, V. Backman, and H. F. Zhang, "Visible-light optical coherence tomography for retinal oximetry," *Opt. Lett.* **38**(11), 1796–1798 (2013).
11. S. Chen, J. Yi, and H. F. Zhang, "Measuring oxygen saturation in retinal and choroidal circulations in rats using visible light optical coherence tomography angiography," *Biomed. Opt. Express* **6**(8), 2840–2853 (2015).
12. N. Bosschaart, G. J. Edelman, M. C. Aalders, T. G. van Leeuwen, and D. J. Faber, "A literature review and novel theoretical approach on the optical properties of whole blood," *Lasers Med. Sci.* **29**(2), 453–479 (2014).
13. Y. Wang, B. A. Bower, J. A. Izatt, O. Tan, and D. Huang, "Retinal blood flow measurement by circumpapillary Fourier domain Doppler optical coherence tomography," *J. Biomed. Opt.* **13**(6), 064003 (2008).
14. G. Seidel, G. Aschinger, C. Singer, S. A. Herzog, M. Weger, A. Haas, R. M. Werkmeister, L. Schmetterer, and G. Garhöfer, "Estimating retinal blood flow velocities by optical coherence tomography," *JAMA Ophthalmol.* **134**(10), 1104–1110 (2016).
15. S. Chen, X. Shu, P. L. Nesper, W. Liu, A. A. Fawzi, and H. F. Zhang, "Retinal oximetry in humans using visible-light optical coherence tomography," *Biomed. Opt. Express* **8**(3), 1415–1429 (2017).
16. P. L. Nesper, B. T. Soetikno, H. F. Zhang, and A. A. Fawzi, "OCT angiography and visible-light OCT in diabetic retinopathy," *Vision Res.* **139**, 191–203 (2017).
17. R. Liu, J. A. Winkelmann, G. Spicer, Y. Zhu, A. Eid, G. A. Ameer, V. Backman, and J. Yi, "Single capillary oximetry and tissue ultrastructural sensing by dual-band dual-scan inverse spectroscopic optical coherence tomography," *Light Sci. Appl.* **7**(1), 57 (2018).
18. S. Pi, A. Camino, M. Zhang, W. Cepurna, G. Liu, D. Huang, J. Morrison, and Y. Jia, "Angiographic and structural imaging using high axial resolution fiber-based visible-light OCT," *Biomed. Opt. Express* **8**(10), 4595–4608 (2017).
19. S. Pi, A. Camino, W. Cepurna, X. Wei, M. Zhang, D. Huang, J. Morrison, and Y. Jia, "Automated spectroscopic retinal oximetry with visible-light optical coherence tomography," *Biomed. Opt. Express* **9**(5), 2056–2067 (2018).

20. A. M. Bickford, "Omnicon F/AIR anesthesia gas filter," <https://ambickford.com/product/fair/>.
21. COOLLAB, "COOLLAB website," www.coollab.net.
22. OceanOptics, "Wavelength Calibration Sources," <https://oceanoptics.com/product-category/wavelength-calibration-sources/>.
23. J. Yi and V. Backman, "Imaging a full set of optical scattering properties of biological tissue by inverse spectroscopic optical coherence tomography," *Opt. Lett.* **37**(21), 4443–4445 (2012).
24. M. Zhang, J. Wang, A. D. Pechauer, T. S. Hwang, S. S. Gao, L. Liu, L. Liu, S. T. Bailey, D. J. Wilson, D. Huang, and Y. Jia, "Advanced image processing for optical coherence tomographic angiography of macular diseases," *Biomed. Opt. Express* **6**(12), 4661–4675 (2015).
25. A. F. Frangi, W. J. Niessen, K. L. Vincken, and M. A. Viergever, "Multiscale vessel enhancement filtering," in *International Conference on Medical Image Computing and Computer-Assisted Intervention*, (Springer, 1998), 130–137.
26. S. P. Chong, T. Zhang, A. Kho, M. T. Bernucci, A. Dubra, and V. J. Srinivasan, "Ultrahigh resolution retinal imaging by visible light OCT with longitudinal achromatization," *Biomed. Opt. Express* **9**(4), 1477–1491 (2018).
27. W. Song, Q. Wei, W. Liu, T. Liu, J. Yi, N. Sheibani, A. A. Fawzi, R. A. Linsenmeier, S. Jiao, and H. F. Zhang, "A combined method to quantify the retinal metabolic rate of oxygen using photoacoustic ophthalmoscopy and optical coherence tomography," *Sci. Rep.* **4**(1), 6525 (2015).
28. J. Yi, W. Liu, S. Chen, V. Backman, N. Sheibani, C. M. Sorenson, A. A. Fawzi, R. A. Linsenmeier, and H. F. Zhang, "Visible light optical coherence tomography measures retinal oxygen metabolic response to systemic oxygenation," *Light Sci. Appl.* **4**(9), e334 (2015).
29. Y. Jia, S. T. Bailey, T. S. Hwang, S. M. McClintic, S. S. Gao, M. E. Pennesi, C. J. Flaxel, A. K. Lauer, D. J. Wilson, and J. Horngger, "Quantitative optical coherence tomography angiography of vascular abnormalities in the living human eye," *Proceedings of the National Academy of Sciences*, 201500185 (2015).
30. M. Zhang, T. S. Hwang, J. P. Campbell, S. T. Bailey, D. J. Wilson, D. Huang, and Y. Jia, "Projection-resolved optical coherence tomographic angiography," *Biomed. Opt. Express* **7**(3), 816–828 (2016).
31. S. Fouquet, O. Vacca, F. Sennlaub, and M. Paques, "The 3D Retinal Capillary Circulation in Pigs Reveals a Predominant Serial Organization," *Invest. Ophthalmol. Vis. Sci.* **58**(13), 5754–5763 (2017).
32. P. L. Nesper and A. A. Fawzi, "Human Parafoveal Capillary Vascular Anatomy and Connectivity Revealed by Optical Coherence Tomography Angiography," *Invest. Ophthalmol. Vis. Sci.* **59**(10), 3858–3867 (2018).
33. C. Leahy, H. Radhakrishnan, G. Weiner, J. L. Goldberg, and V. J. Srinivasan, "Mapping the 3D connectivity of the rat inner retinal vascular network using OCT angiography," *Invest. Ophthalmol. Vis. Sci.* **56**(10), 5785–5793 (2015).
34. M. Paques, R. Tadayoni, R. Sercombe, P. Laurent, O. Genevois, A. Gaudric, and E. Vicaut, "Structural and hemodynamic analysis of the mouse retinal microcirculation," *Invest. Ophthalmol. Vis. Sci.* **44**(11), 4960–4967 (2003).
35. S. T. Garrity, M. Paques, A. Gaudric, K. B. Freund, and D. Sarraf, "Considerations in the Understanding of Venous Outflow in the Retinal Capillary Plexus," *Retina* **37**(10), 1809–1812 (2017).
36. T. E. Kornfield and E. A. Newman, "Measurement of Retinal Blood Flow Using Fluorescently Labeled Red Blood Cells," *eNeuro* **2**(2), ENEURO0005 (2015).
37. V. J. Srinivasan and H. Radhakrishnan, "Total average blood flow and angiography in the rat retina," *J. Biomed. Opt.* **18**(7), 076025 (2013).
38. E. M. Kohner, A. M. Hamilton, S. J. Saunders, B. A. Sutcliffe, and C. J. Bulpitt, "The retinal blood flow in diabetes," *Diabetologia* **11**(1), 27–33 (1975).
39. S. E. Bursell, A. C. Clermont, B. T. Kinsley, D. C. Simonson, L. M. Aiello, and H. A. Wolpert, "Retinal blood flow changes in patients with insulin-dependent diabetes mellitus and no diabetic retinopathy," *Invest. Ophthalmol. Vis. Sci.* **37**(5), 886–897 (1996).
40. F. C. Delori, R. H. Webb, and D. H. Sliney, "Maximum permissible exposures for ocular safety (ANSI 2000), with emphasis on ophthalmic devices," *J. Opt. Soc. Am. A* **24**(5), 1250–1265 (2007).
41. S. P. Chong, M. Bernucci, H. Radhakrishnan, and V. J. Srinivasan, "Structural and functional human retinal imaging with a fiber-based visible light OCT ophthalmoscope," *Biomed. Opt. Express* **8**(1), 323–337 (2017).
42. S. Chen, X. Shu, P. L. Nesper, W. Liu, A. A. Fawzi, and H. F. Zhang, "Retinal oximetry in humans using visible-light optical coherence tomography [Invited]," *Biomed. Opt. Express* **8**(3), 1415–1429 (2017).
43. C. E. Riva, E. Logean, and B. Falsini, "Visually evoked hemodynamical response and assessment of neurovascular coupling in the optic nerve and retina," *Prog. Retin. Eye Res.* **24**(2), 183–215 (2005).
44. R. D. Braun, R. A. Linsenmeier, and T. K. Goldstick, "Oxygen consumption in the inner and outer retina of the cat," *Invest. Ophthalmol. Vis. Sci.* **36**(3), 542–554 (1995).
45. R. Liu, G. Spicer, S. Chen, H. F. Zhang, J. Yi, and V. Backman, "Theoretical model for optical oximetry at the capillary level: exploring hemoglobin oxygen saturation through backscattering of single red blood cells," *J. Biomed. Opt.* **22**(2), 025002 (2017).

Rodent retinal circulation organization and oxygen metabolism revealed by visible-light optical coherence tomography

Pi, Shaohua; Camino, Acner; Wei, Xiang; Simonett, Joseph; Cepurna, William;
Huang, David; Morrison, John C.; Jia, Yali

01 Yukun Guo

Page 3

23/10/2020 20:39